Preprints of the 19th World Congress
The International Federation of Automatic Control
Cape Town, South Africa. August 24-29, 2014

Phase-locked Loop-based Proportional Integral Control for Spiral Scanning in an Atomic Force Microscope

H. Habibullah * **H. R. Pota** * **I. R. Petersen** *

* *Authors are with the School of EIT, University of New South Wales, Canberra, ACT-2612, Australia. (e-mail: h.habib@student.adfa.edu.au, h.pota@adfa.edu.au, i.petersen@adfa.edu.au).*

Abstract: The design of a phase-locked loop (PLL)-based proportional integral (PI) controller for improving the spiral scanning of a piezoelectric tube scanner (PTS), used in an atomic force microscope (AFM), is demonstrated in this paper. Spiral motion of the PTS for scanning of material surfaces or biological samples using an AFM is achieved by applying two sinusoidal signals with a 90 degree phase-shift and of varying amplitudes to the X and Y-axes of the scanner. If there is an exact 90-degree phase shift between the sinusoidal displacements of the two scanner axes, a true circular image is generated. Otherwise, the image will distort into an elliptical shape, which can lead to missing data points or changes in the lattice structure of the sample surface to be scanned. The phase error between the X and Y-axes positions increases with increasing scanning speeds. In this proposed control scheme, the phase error between the displacements of the two lateral axes of the scanner is measured by a phase detector and is minimized using a PI controller. Experimental results for reference tracking and imaging performance confirm the efficiency of the proposed control scheme.

Keywords: Atomic force microscopy, phase-locked loop, spiral scanning, nanopositioning control.

1. INTRODUCTION

Atomic force microscopes (AFMs) are becoming the workhorses of scanning probe technology as these are being used to measure the topography of material surfaces with an atomic resolution. As a result of increased demand for precision measurements, metrology of surface finish is of great interest to the surface scientists Young et al. [Mar. 1972], Vorburger et al. [1997]. The AFM measures the surface topography of materials and biological samples by moving a sharp probe over a surface, resulting in atomic resolution images of both electrically conductive and non-conductive surfaces Kim et al. [2005], Drake et al. [1989], Binnig et al. [1986]. A piezoelectric tube actuator (PTA) is used in AFMs and the advantages of piezoelectric materials (PZM) are they offer nanometer range motion without backlash, high stiffness, and fast response time Ping and Musa [1995]. The AFM has limitations in its high speed scanning because of the nature of piezoelectric tube scanners (PTSs) as it involves effects of hysteresis, creep, and vibration at high frequencies Ben-Mrad and Hu [2002].

Imaging the surface of a sample with a commercially available AFM is achieved by applying a small, gradually increasing gradient staircase or ramp signal in the y direction while concurrently applying a triangular signal along the x direction. One of the main drawbacks of this scanning method is that its spatial resolution is poor as the triangular signal contains all of the odd harmonics of the fundamental frequency. In raster scanning, the scanning speed is usually limited to 1-10 percent of the first resonant frequency of the PTS Mahmood and Moheimani [2009b]. When a triangular signal is input to the PTS, one of the high-frequency harmonics excites the resonance and a distorted triangular signal is produced at the free end of the PTS along the X-axis which generates a distorted image. In the SPM and other scanner devices, such as selective laser sintering machines (SLSs), tracking a triangular signal is a major challenge Zhiqiang et al. [May. 2007].

Line by line (raster) scanning produces images with deformed atomic lattices, which leads to misinterpretations of the original data while drifting occurs which may cause the image to be oblique. For example, a square lattice becomes rhombohedral and since this is a well-known structure, one can draw the wrong conclusions. To avoid this, spiral scanning approaches have been introduced in Wang et al. [Jul. 2010], Mahmood and Moheimani [2009a], Kotsopoulos et al. [Aug. 28–Sep. 02, 2011], Mahmood et al. [2011] for fast imaging using the AFM. In Hung [2010] a spiral scanning method is reported as a replacement for raster scanning and in this scanning two challenges are mentioned: the first challenge is the uniform distribution of sampling points in the 2-D plane and the second is a relatively constant linear speed. A detailed image construction procedure is also described in Hung [2010] but the images have a higher distortion as compared to the images scanned using the proposed scheme. A specially designed AFM head is used for spiral scanning in Wei et al. [2007] where the AFM head is mounted on a spindle for generating rotational motion and a turning machine is used to turn a sample, but it is hard to maintain the relative position of the head and the sample. A fast spiral scanning technique is also reported in Hoge et al. [1997] for medical magnetic resonance imaging (MRI).

As an alternative to traditional raster scanning, an approach of gradient pulsing using a spiral line is implemented in this paper. In it, the entire frequency domain is uniformly covered

⋆ This work was supported by the Australian Research Council.

by a form of spiral scanning whereby a circular symmetrical area for fast AFM imaging is obtained, which is different from that determined from raster scanning, is obtained. Externally generated cosine and sine waves of slowly varying amplitudes are applied to the PTA scanner's X and Y-axes to force it to move along spiral lines with varying instantaneous radii. The resultant spiral signal has a low-frequency content which moves slowly over time and regulates the tracking performance through continuous high-frequency imaging. These generated spirals are called Archimedean spirals Kotsopoulos and Antonakopoulos [2010]. The distance between two consecutive lines in the spiral is known as the pitch which has the property of being constant over the sample surface that makes it possible to uniformly scan the surface without missing any surface information Ahn et al. [1986].

Using open-loop scanning, it is not possible to scan in a uniformly circular area because of the hysteresis effect which leads to inaccurate tracking as it generates amplitude-dependent phase shifts that reduce the effectiveness of open-loop control. As a result, it limits the precision motion that can be obtained using the PTS Ben-Mrad and Hu [2002]. In Habibullah et al. [doi=10.1109/ASCC.2013.6606378, 2013] an internal sinusoidal reference model-based optimal LQG controller is designed and implemented on an AFM to track a reference sinusoidal signal but it leads to a phase error due to the high frequency dynamics of the PTS. In this proposed scheme, a phase-locked loop (PLL)-based PI control is designed and implemented on the AFM to compensate for phase errors between the X and Y positions. A phase detector is used to measure phase errors between sinusoids. A PI controller is used to reduce this error. Almost true spiral and undistorted images are demonstrated for comparison with the raster scanned images using the in-built AFM PI controller.

The remainder of this paper is organized as follows: Section 2 presents the spiral generation procedure; Section 3 explains the modeling of the PTS; Section 4 discusses the controller design procedure; Section 5 presents the performance of the controller, improvement of the scanning speed, and quality of images; and Section 6 provides conclusions.

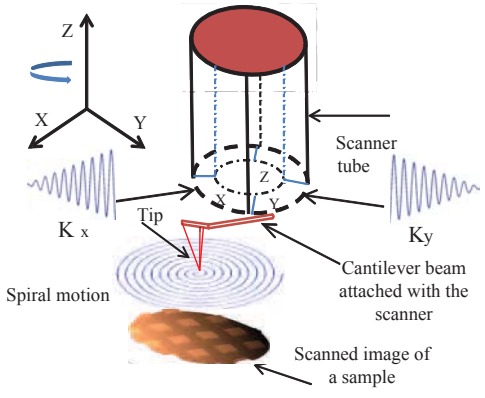

Fig. 1. A schematic view of the PTS.

2. BASIC MATHEMATICS FOR SPIRAL GENERATION

The most popular 3-D Fourier imaging algorithm with three time varying gradient fields is:

$$G(t) = \iiint \sigma(x,y,z)\exp\ [i\gamma \int_0^t xG_x(t) + yG_y(t)dt] \exp(\frac{t}{T_2})dxdydz \quad (1)$$

where, $G(t)$ is the free induction decay signal (FID), $\sigma(x,y,z)$ is the spin density distribution. $G_x(t), G_y(t)$, and $G_z(t)$ are the time-varying gradient fields of the x, y, and z coordinates, respectively. The exponential term $exp(t/T_2)$ is the T_2 decay term that often appears as a limiting factor in high-resolution imaging.

The general 3-D imaging equation can be converted to 2-D forms for analysis and the T_2 decay term can be ignored for simplicity Ahn et al. [1986]. The FID signal obtained for a 2-D plane at $z = z_0$ is:

$$G(t) = \iint \sigma(x,y,z_0)\exp\ [i \int_0^t xk_x(t) + yk_y(t)]dxdy; \simeq G((k_x,k_x) \quad (2)$$

where,

and

$$k_x = \gamma \int_0^t G_x(t)dt; \quad k_y = \gamma \int_0^t G_y(t)dt. \quad (3)$$

From (2) and (3) it can be shown that, $\sigma(x,y)$ and $G(k_x,k_y)$ are a Fourier transform pair. The following two sinusoidal signals simultaneously applied to the X and Y-axes will result in a set of circularly symmetrical concentric circles with different instantaneous radii:

$$k_x(t) = \gamma\eta_i(t)\cos\omega t \quad k_y(t) = \gamma\eta_i(t)\sin\omega t \quad (4)$$

where, $\eta_i(t)$ is the discrete amplitude at time t and ω is frequency of the sine wave.

Continuous rather than discrete circles, i.e, complete spiral motions can be obtained from simple modification of (4), which would be easier to implement in a physical system as:

$$k_x(t) = Rcos\omega t \quad k_y(t) = Rsin\omega t \quad (5)$$

where, $R = \gamma\eta t$ is the instantaneous radius of the spiral at time t. Simultaneous application of these two signals in (5) results in continuously increasing circles, which create complete spiral positioning on a sample surface, as shown in Fig. 1.

3. MODELING OF THE PTS

In the design of the proposed control scheme, the PTS is modeled as a single-input single-output (SISO) system. An experimental frequency response is obtained using a dual-channel HP35665A dynamic signal analyser (SA). In this work, our experimental setup consists of the NT-MDT Ntegra scanning probe microscope (SPM) that is configured as an AFM. The experimental setup contains some other parts such as a signal access module (SAM), control electronics, a vibration isolator, and a computer to operate the NOVA software. Other accessories are a DSP dSPACE board and high-voltage amplifier (HVA) with a constant gain of 15 which supplies power to the X, Y, and Z-PTSs using the SAM as an intermediate device. The scanner is a NT-MDT Sm836cl PI type which scans by head in the constant force contact mode in Mironov [2004]. The (X, Y, Z) scanning range is 100μm$\times100\mu$m$\times10\mu$m and the

resonant frequency for both X and Y-axes is 700-800 Hz, and 5 kHz for the Z-PTS that performs the X, Y, and Z positioning in the AFM. Displacement measurements of the X, Y, and Z-PTS are obtained from capacitive position sensors incorporated with the AFM. The experimental setup is shown in Fig. 2 and an image of our laboratory setup can be found in Habibullah et al. [2013a]. The frequency responses generated in the SA are

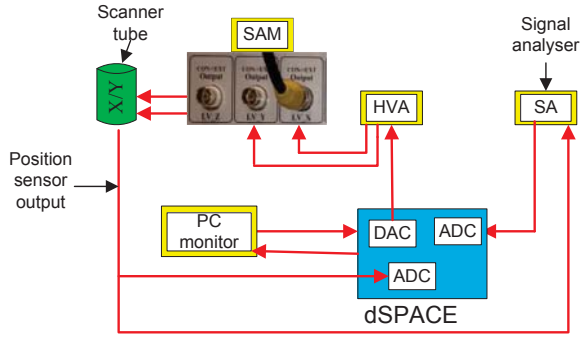

Fig. 2. Block diagram of experimental setup used in the AFM positioning.

processed in MATLAB and using the prediction error method (PEM), a system model is obtained Ljung [2002], Habibullah et al. [2013b], Kabaila [1983]. The best-fit model frequency responses for the X and Y-PTSs are shown in Fig. 3.

The following state-space model is found to be the best fit for the X-PTS, as illustrated in Fig. 3(a) and the first resonant mode is at about 683 Hz and the second mode is at 1090 Hz:

$$\dot{x_x} = a_x x_x + b_x u_x; \tag{6}$$

$$y_x = c_x x_x + d_x u_x; \tag{7}$$

$$a_y = \begin{bmatrix} 27.6 & -4775.2 & 1859.7 & -281.6 & 26.7 \\ 3883.6 & -161.2 & 1140.4 & -354.6 & 2479.6 \\ -173.3 & -358.1 & -778.1 & 1990.5 & -6309.8 \\ 19.9 & -31.2 & -1177.5 & -86 & 5968.9 \\ -8.3 & -165.2 & 1874.1 & -5229.9 & -99.5 \end{bmatrix};$$

$$b_y = [9.6681\ 9.9318\ 13.0409\ 2.2707\ 0.7973]';$$

$$c_y = [23.7551\ 21.3737\ -45.7398\ 14.9963\ -67.6122];$$

$$d_y = [0].$$

Similarly, the following state-space model is found to be the best fit for the Y-PTS, as illustrated in Fig. 3(b) where the first resonant mode of the PTS is at about to 683 Hz and second mode at 1100 Hz:

$$\dot{x_y} = a_y x_y + b_y u_y; \tag{8}$$

$$y_y = c_y x_y + d_y u_y; \tag{9}$$

$$a_y = \begin{bmatrix} 16.4 & 4754.1 & -1812.4 & -447.6 & 52 \\ -3857.8 & -142.4 & 995.4 & 190.1 & -2370.7 \\ 102.3 & -256.4 & -833.3 & -1332.2 & 5671.2 \\ 12 & 26.3 & 825.8 & -62.8 & 6804.2 \\ -2.8 & 105.4 & -1317.5 & -5684.1 & -166.3 \end{bmatrix};$$

$$b_y = [11.6492\ -10.6956\ -13.1857\ 0.6865\ 0.8459]';$$

$$c_y = [25.3332\ -20.8563\ 45.5930\ 12.5395\ -68.2417];$$

$$d_y = [0].$$

In Fig. 3, we can see that both of these PTS plants have a 180° phase shift at low frequencies and zeros in the right half plane.

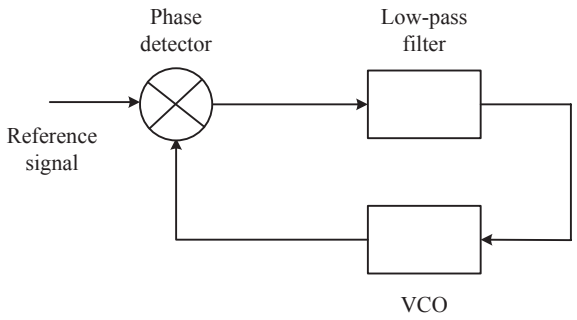

Fig. 4. A basic PLL block diagram.

4. CONTROLLER DESIGN

4.1 Design of PLL

A phase-locked loop (PLL) is used in communication systems where frequency synchronization is required. The basic architecture of a PLL is shown in Fig. 4. The phase detector multiplies two sinusoidal signals Pota [2005]. One is the reference sinusoid and the other one is the output from the voltage controlled oscillator (VCO) as:

$$\begin{aligned} K_x &= K_i \sin(\omega_i t + \pi/2); \\ K_y &= K_0 \sin(\omega_0 t + \phi); \end{aligned} \tag{10}$$

where K_i and K_0 are the amplitudes of the reference signal and output of the VCO. ω_i, ω_0 are the frequencies and $\pi/2$, ϕ are the phases of the reference and VCO output signals, respectively. The output of the phase detector is composed of a double frequency signal and error signal between the two, as described:

$$\begin{aligned} K_e &= K_x \times K_y; \\ &= \frac{K_i K_0}{2} \cos(\pi/2 - \phi) - \cos(2\omega_i t + \pi/2 + \phi); \end{aligned} \tag{11}$$

where K_e is the error between the input and output. K_e is filtered through a low-pass filter, as a result double frequency component is eliminated and the error signal is:

$$K_e = \frac{K_i K_0}{2} \sin(\phi); \tag{12}$$

Equation (12) describing a nonlinear PLL. For simplicity in the stability analysis, this is linearized by considering the phase error (ϕ) to be very small. Therefore the linearized PLL is:

$$K_e = \frac{K_i K_0}{2} \phi; \tag{13}$$

For this proposed system $K_i = K_0$ and $\omega_i = \omega_0$. A block diagram of a linearized PLL combined with a PI controller is shown in Fig. 5. The configuration is similar to the PLL, depicted in Fig. 4, except that the VCO is replaced with the Y-PTS Djatmiko and Sutopo [Mar, 2001], Zhan et al. [Jan. 2001]. A sinusoidal signal with varying amplitude comes out from the X-PTS and another sinusoidal signal with a 90 degree phase shift comes out from the Y-PTS and are compared in the phase detector to measure the phase error.

4.2 Design of the Low-pass Filter

The purpose of designing a low-pass filter for the PLL loop is to eliminate the high-frequency component of the phase detector's outputs and to generate a low-frequency error signal which is to be controlled by a well tuned PI controller. A well-known low-pass filter of the following form is used in this proposed work:

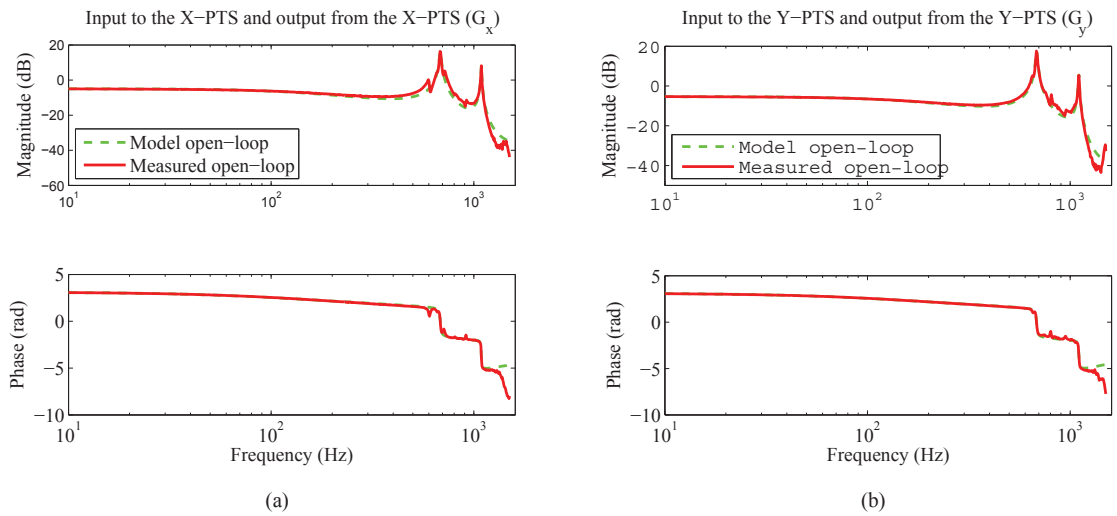

Fig. 3. Frequency response plots of measured and identified system models for (a) input to the X-PTS and output from the X position sensor (b) input to the Y-PTS and output from the Y position sensor.

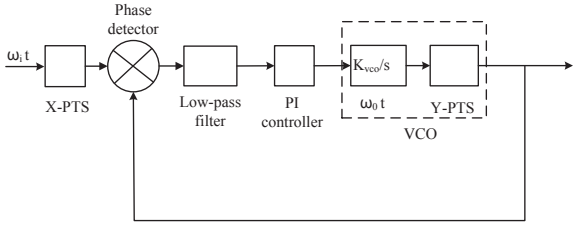

Fig. 5. A block diagram of a linearized PLL with PI controller.

$$F(s) = \frac{k_f}{s^3 + 3\omega_c s^2 + 3{\omega_c}^2 s + {\omega_c}^3}; \tag{14}$$

where K_f is the filter gain, ω_c is the corner frequency of the filter. The filter parameters are chosen based on the operating frequency of the system. In our case we have set different frequencies to scan at different speeds.

4.3 Design of PI Controller

In this proposed scheme the following form of PI controller is considered to minimize phase error (between the position sensor outputs of the X and Y-PTS) which comes out of the phase detector.

$$G_c(s) = \frac{K_p s + K_I}{s}; \tag{15}$$

where K_p and K_I are the proportional and integral gains. In spiral scanning for an AFM, to make a true spiral it is necessary to ensure a 90 degree phase shift between the X and Y-PTS output sinusoids. Due to the nonlinear behavior of the PTS scanner, in open-loop applications there is a problem in tracking a reference sinusoid and even at low frequencies it experiencing huge amount of phase shift. This phase error is measured by the phase detector and compensated by using a PI controller. A good dynamic response and stability are required for the control system. According to classical control theory: a linearized PLL with PI controller has zero steady-state error because it forms a type-II system. However this error is experienced for a step change in the derivative of frequency. A trade-off is used to reduce this steady-state error by choosing the gains K_p and K_I. In this design, the selected value of K_p is 56 and K_I is 478. A

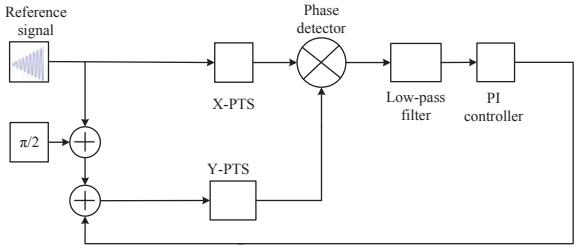

Fig. 6. Block diagram for implementation of the proposed controller.

block diagram for the closed-loop implementation is shown in Fig. 6.

5. EXPERIMENTAL RESULTS

5.1 Tracking Performance

The proposed PLL-based PI controller is implemented on the AFM and a set of experimental tracking performance results are presented in Fig. 7. Fig. 7(a) and (b) show the tracking of sine and cosine (voltage) signals. Fig. 7(c) shows the tracking of a spiral trajectory. Fig. 7 (d) shows the phase shifting between sine and cosine waves, all are at 10 Hz frequency. From these figures, it can be observed that the proposed scheme has achieved a good tracking of reference trajectories and maintained a 90 degree phase shift between the two sinusoids. In Fig. 7 (d), a 0.02 s constant delay between the consecutive peaks is confirmed along the sinusoidal trajectories at 10 Hz. Similarly, Fig. 7(e), (f) show the sinusoidal tracking at 30 Hz, Fig. 7(g) shows the spiral tracking and Fig. 7(h) shows phase shifting between the sinusoids at the same frequency. At 30 Hz frequency again a constant 0.009 s time delay is confirmed between the consecutive peaks of the sinusoidal signals along the trajectory.

5.2 Image Scanning Performance

The tracking performance of the proposed controller shows that the PTS scanner achieves good spiral positioning when

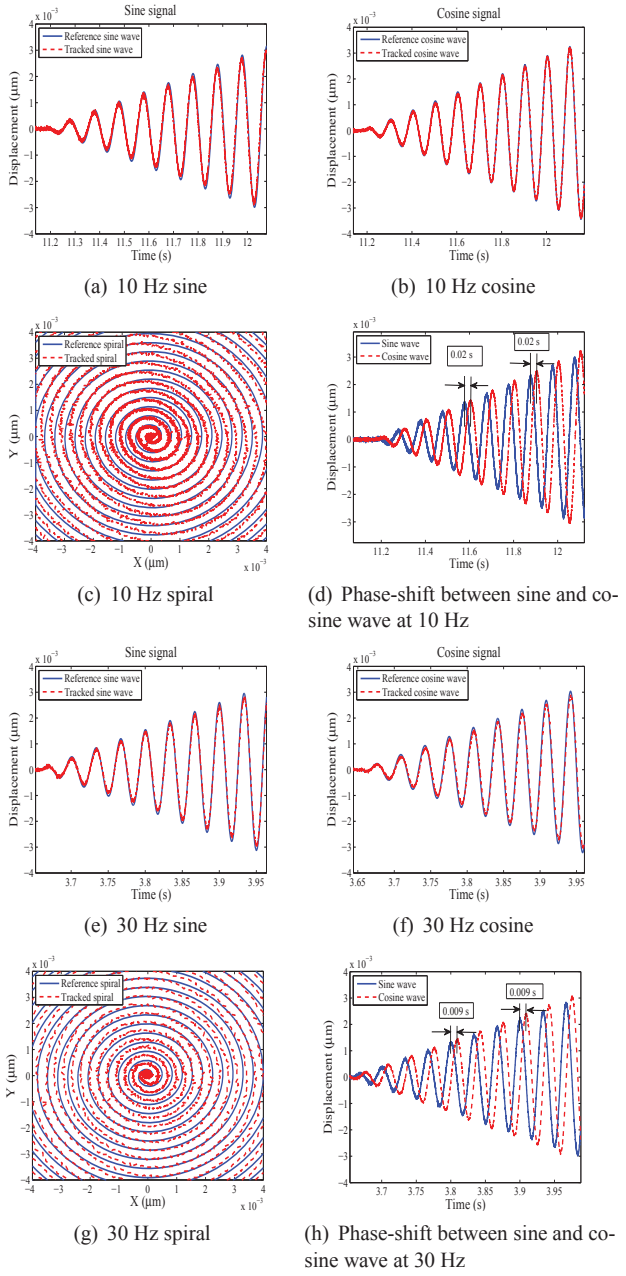

(a) 10 Hz sine (b) 10 Hz cosine

(c) 10 Hz spiral (d) Phase-shift between sine and cosine wave at 10 Hz

(e) 30 Hz sine (f) 30 Hz cosine

(g) 30 Hz spiral (h) Phase-shift between sine and cosine wave at 30 Hz

Fig. 7. Tracking performance of the proposed controller at different frequencies.

applied to the AFM for the spiral scanning of a TGQ1 standard calibration grating with a 20 nm surface height and 3 μm pitch (period). The instantaneous radius of the spiral is maintained at 6 μm and 512 lines, i.e., the diameter of the image contains 512 pixels. A constant-force contact mode AFM imaging technique is set up for spiral scanning and the Z deflection is recorded to construct the spiral image. The results are observed by implementing the proposed controller in the X and Y-axes with the help of the real-time dSPACE system. The Z axis is controlled using the in-built AFM PI controller.

The generated spiral images scanned at 10, 30, 60, and 120 Hz are shown in Fig. 8(a)–(d). One point to note is that 2D planes of the images are not corrected for flatness. There are some uneven illuminations in them caused by imperfections, i.e., small inclination of the sample surface, dust and additional physical properties. A set of raster scanned images using the

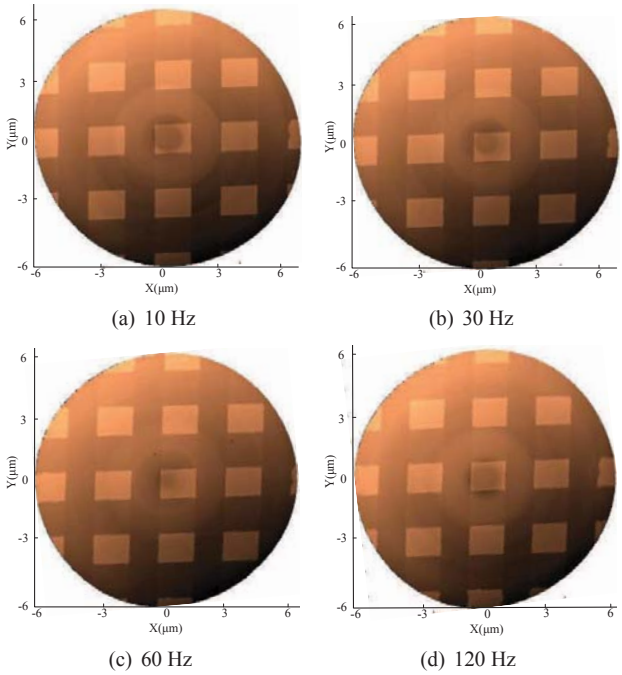

(a) 10 Hz (b) 30 Hz

(c) 60 Hz (d) 120 Hz

Fig. 8. Spiral scanned images using proposed controller at different frequencies.

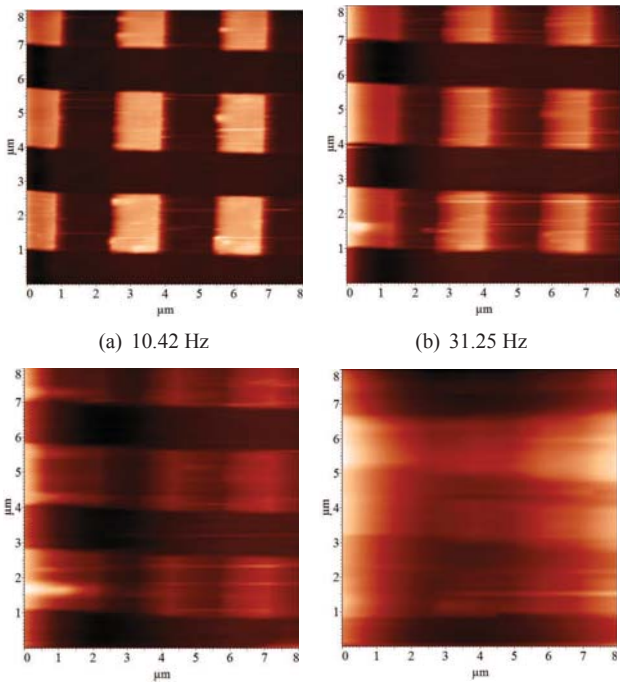

(a) 10.42 Hz (b) 31.25 Hz

(c) 62.5 Hz (d) 125 Hz

Fig. 9. Raster scanned images using the AFM PI controller at different frequencies.

AFM PI controller at 10.42, 31.25, 62.5, and 125 Hz (the reason for choosing these scanning frequencies is that they are the only ones above 10 Hz permitted by the AFM NT-MDT software) are presented in Fig. 9(a)–(d) for comparison with the spiral scanned images. The spiral images are observed to be undistorted and follow the regular profile of the calibration grating. In contrast, the raster scanned images using the standard AFM PI controller become distorted and are affected by the induced vibration and high-speed dynamics of the PTS as the scanning

frequency increases, as can be seen in Fig. 9(c) and (d). The spiral scanned image in Fig. 8(d) at 120 Hz has a circular wrapping effect but still better than the image using the in-built AFM PI controller in Fig. 9(d).

6. CONCLUSIONS

A PLL-based PI controller is implemented on an AFM to achieve better quality spiral images reducing phase errors between the X and Y position of the sinusoidal signals. The proposed control scheme has achieved a good tracking of sinusoidal signals and produced a regular spiral area rather than a distorted spiral like an elliptical shape. The imaging performance using the proposed scheme depicts better imaging artifacts than the raster scanned image using the in-built AFM PI controller. However, the images scanned at the frequencies above 60 Hz, a little distortion is experienced.

ACKNOWLEDGEMENTS

The authors would like to thank Mr. Shane Brandon who helps in the experimental works.

REFERENCES

Ahn, C.B., Kim, J.H., and Cho, Z.H. (1986). High-speed spiral-scan echo planar NMR imaging-i. *IEEE Transactions on Medical Imaging*, 5(1), 2–7.

Ben-Mrad, R. and Hu, H. (2002). A model for voltage-to-displacement dynamics in piezoceramic actuators subject to dynamic-voltage excitations. *IEEE/ASME Transactions on Mechatronics*, 7(4), 479–489.

Binnig, G., Quate, C.F., and Gerber, C. (1986). Atomic force microscope. *Phys. Rev. Lett.*, 56, issue 9, 930–933.

Djatmiko, W. and Sutopo, B. (Mar, 2001). Speed control DC motor under varying load using phase-locked loop system. In *Proc. of the International Conf. on Electrical, Electronics, Communication, and Information CECI*.

Drake, B., Prater, C., Weisenhorn, A., Gould, S., Albrecht, T., Quate, C., Cannell, D., Hansma, H., and Hansma, P. (1989). Imaging crystals, polymers, and processes in water with the atomic force microscope. *Science*, 243(4898), 1586–1589.

Habibullah, Pota, H.R., and Petersen, I.R. (doi=10.1109/ASCC.2013.6606378, 2013). Developing a spiral scanning method using atomic force microscopy. In *9th Asian Control Conference ASCC*, 1–6.

Habibullah, H., Pota, H.R., Petersen, I.R., and Rana, M.S. (2013a). Creep, hysteresis, and cross-coupling reduction in the high-precision positioning of the piezoelectric scanner stage of an atomic force microscope. *IEEE Transactions on Nanotechnology*, 12(6), 1125–1134.

Habibullah, H., Pota, H.R., Petersen, I.R., and Rana, M.S. (2013b). Tracking of triangular reference signals using LQG controllers for lateral positioning of an AFM scanner stage. *IEEE/ASME Transactions on Mechatronics*, In press, DOI: 10.1109/TMECH.2013.2270560(99), 1–10. doi: 10.1109/TMECH.2013.2270560.

Hoge, R.D., Kwan, R.K.S., and Bruce Pike, G. (1997). Density compensation functions for spiral MRI. *Magnetic Resonance in Medicine*, 38, issue 1, 117–128.

Hung, S.K. (2010). Spiral scanning method for atomic force microscopy. *Journal of Nanoscience and Nanotechnology*, 10(7), 4511–4516.

Kabaila, P. (1983). On output-error methods for system identification. *IEEE Transactions on Automatic Control*, 28, no. 1, 12–23.

Kim, B., Pyrgiotakis, G., Sauers, J., and Sigmund, W.M. (2005). The effect of monolayers alkyl chain length on atomic force microscopy anodization lithography. *Colloids and Surfaces A: Physicochemical and Engineering Aspects*, 253(10–3), 23–26.

Kotsopoulos, A.G. and Antonakopoulos, T.A. (2010). Nanopositioning using the spiral of archimedes: The probe-based storage case. *Mechatronics*, 20(2), 273–280.

Kotsopoulos, A.G., Pantazi, A., Sebastian, A., and Antonakopoulos, T. (Aug. 28–Sep. 02, 2011). High-speed spiral nanopositioning. In *Proceedings of the 18th IFAC World Congress*, 2018–2023.

Ljung, L. (2002). Prediction error estimation methods. *Circuits, Systems and Signal Processing*, 21, issue 1, 11–21.

Mahmood, I.A., Moheimani, S.O.R., and Bhikkaji, B. (2011). A new scanning method for fast atomic force microscopy. *Nanotechnology, IEEE Transactions on*, 10(2), 203–216.

Mahmood, I.A. and Moheimani, S.O.R. (2009a). Fast spiral-scan atomic force microscopy. *IOP science, Nanotechnology*, 20, no. 36, 365503 (4 pages).

Mahmood, I.A. and Moheimani, S.O.R. (2009b). Making a commercial atomic force microscope more accurate and faster using positive position feedback control. *Review of Scientific Instruments*, 80(6), 063705(1)–063705(8). doi: 10.1063/1.3155790.

Mironov, V.L. (2004). *Fundamentals of Atomic Force Microscopy*.

Ping, G. and Musa, J. (1995). Modeling hysteresis in piezoceramic actuators. *Precision Engineering*, 17(3), 211–221.

Pota, H.R. (2005). *Phase-Locked Loop*.

Vorburger, T.V., Dagata, J.A., Wilkening, G., Lizuka, K., Thwaite, E.G., and Lonardo, P. (1997). Industrial uses of STM, and AFM. *CIRP, Annals–Manufacturing Technology*, 46(2), 597–620.

Wang, A.J., Wang, J., Hou, Y., and Lu, Q. (Jul. 2010). Self-manifestation and universal correction of image distortion in scanning tunneling microscopy with spiral scan. *Review of Scientific Instruments*, 81(Issue 7), 074101(5).

Wei, G., Jun, A., Bing-Feng, J., and Satoshi, K. (2007). Surface profile measurement of a sinusoidal grid using an atomic force microscope on a diamond turning machine. *Precision Engineering-journal of The International Societies for Precision Engineering and Nanotechnology*, 31, 304–309.

Young, R., Ward, J., and Scire, F. (Mar. 1972). The topografiner: An instrument for measuring surface microtopography. *Review of Scientific Instruments*, 43(7), 999–1011.

Zhan, C., Fitzer, C., Ramachandaramurthy, V.K., Arulampalam, A., Barnes, M., and Jenkins, N. (Jan. 2001). Software phase-locked loop applied to dynamic voltage restorer (DVR). In *IEEE Power Engineering Society Winter Meeting*, volume 3, 1033–1038 vol.3.

Zhiqiang, D., Zude, Z., Wu, A., and Youping, C. (May. 2007). A linear drive system for the dynamic focus module of SLS machines. *The International Journal of Advanced Manufacturing Technology*, 32, 1211–1216.